Gravitational waves through the cosmic web

Garoffolo, A.

3

Synergies with galaxy surveys

We investigate the synergy of upcoming galaxy surveys and gravitational wave (GW) experiments in constraining late-time cosmology, examining the cross-correlations between the weak lensing of gravitational waves (GW-WL) and the galaxy fields. Without focusing on any specific GW detector configuration, we benchmark the requirements for the high precision measurement of cosmological parameters by considering several scenarios, both in ΛCDM and alternative DE theories. We find that, in some of the explored setups, GW-WL contributes to the galaxy signal by doubling the accuracy on non-ΛCDM parameters. Though the most extreme cases presented here are likely beyond the observational capabilities, we show nonetheless that – provided that enough statistics of events can be accumulated – GW-WL offers the potential to become a cosmological probe complementary to large-scale structure surveys.

Keywords: Gravitational waves, weak lensing, dark energy, cross-correlations

Based on: *Prospects of testing late-time cosmology with weak lensing of gravitational waves and galaxy surveys*

A. Balaudo, A. Garoffolo, M. Martinelli, S. Mukherjee, A. Silvestri,

e-Print: 2210.06398 [astro-ph.CO]

3.1. Introduction

The historical direct detection of a gravitational wave (GW) by the LIGO-Virgo collaboration in 2015 [1], marked the beginning of a series of observing campaigns that led to the detection of around one hundred sources [16, 258, 259]. In the near future, the KAGRA interferometer [260] will join LIGO-Virgo in their observing runs, while the space-based interferometer LISA [25] is expected to launch in the late '30s. The third generation of ground-based GW detectors will see light with the network of Einstein Telescope (ET) [18] and Cosmic Explorer (CE) [19], drastically improving the sensitivity to GW signals and measure hundreds of thousands of events over 10 years of observations. While GW170817 led the way, allowing the first GW measurement of the Hubble constant [205], multi-band GW observations will open a new promising window in observational cosmology, which can be used both to trace different GW sources populations, and to investigate the matter structures along the line of sight. Meanwhile, the intense worldwide effort towards mapping the Universe via galaxy and weak lensing surveys has started to deliver large-scale structure (LSS) data of unprecedented precision, such as those provided by KiDS [103, 104] and DES [101, 102] collaborations. With Stage IV missions (*Euclid* [105], the Vera C. Rubin Observatory [12, 106, 107] and Nancy Grace Roman Space Telescope [108]) we will see a paradigm shift in the volume of data available. This will lead to a new level of scrutiny of the standard model of cosmology: ΛCDM, introduced in Section 1.1. This model successfully describes the Universe in terms of few parameters, yet the rise of precision cosmology has seen the emergence of some tensions between datasets when interpreted within it [13, 14], which could signal the first cracks in ΛCDM as we are achieving a new level of precision in the measurement of its parameters [15].

With the ongoing/upcoming cosmological surveys, we have the opportunity to probe gravity on cosmological scales, and shed light, for instance, on the nature of dark energy. We focus on extensions of ΛCDM that address the phenomenon of cosmic acceleration by means of a scalar dynamical dark energy component or modifying the laws of gravity on large scales [52, 54], as in Section 1.2. In order to further tighten the constraints coming from wide surveys that combine galaxy clustering (GC) and weak lensing (WL) on the cosmological parameters, it will be crucial to bring in new probes able to provide independent measurements and also break degeneracies between the various effects participating in the growth of cosmic structures. Multi-band GW observations are very interesting to this extent, as they offer complementary probes, characterized by a different set of systematics with respect to galaxy surveys.

The dynamics of GWs depends on the extended parameters on two level: explicitly, if they enter directly their propagation equation (e.g. Eq. (1.103)), and implicitly, via a different expansion rate of the Universe and growth of gravitational potentials (see discussion after Eq. (1.114)). On the contrary, the dynamics of photons is not explicitly modified in DE theories such as (1.62), opening the possibility of gaining con-

straining power through probes that combine electromagnetic and GW signals. One example of such degeneracy breaking is the cosmological friction term, the *Hubble drag*, which gets modified for GWs (see, e.g. Eqs. (1.74) or (1.103)) when the theory displays a running Planck's Mass, but not for photons. This results in a difference between the luminosity distance inferred from electromagnetic sources and the one inferred from the amplitude of GWs, as stated in Eq. (1.105), and widely addressed in literature as a mean to test the theory of gravity [122, 123, 183–191].

In this Chapter, we focus on the weak lensing (GW-WL) contribution to the GW's luminosity distance fluctuations (Eq. (1.112)) and explore its potentialities in constraining cosmological parameters. For high enough redshift sources ($z \gtrsim 1.5$), GW-WL can cause up to $\sim 5\%$ distortion in the GW strain, posing a serious limitation to the precision with which the true luminosity distance of the sources is measured [157, 225, 261]. More interestingly, and similarly to what done in Chapter 2, it can also be exploited as signal [262], especially when cross-correlated with galaxies [177, 223, 263], CMB lensing [222], HI intensity mapping [264, 265] and other GW probes [266, 267], since both messengers span the same large-scale structures when propagating. We introduce a lensing convergence estimator for GWs, which contains explicitly a contribution from the conformal coupling, $M_P[\varphi]$, characteristic of scalar-tensor theories, thus maximizing the constraining power on cosmological parameters when cross correlating GW-WL with the galaxy fields (GC and WL). Without focusing on a specific GW detector, with its noise and sensitivity, we investigate the requirements, in terms of number of sources and detection precision, for GW-WL to contribute significantly to the GC+WL signal of galaxies.

3.2. Gravitational waves observation

As already discussed in Section 1.4.2, in the DE theories described by the action (1.62), the non-minimal coupling $M_P[\varphi]$ induces an additional dissipation term in the equation for propagation of GWs on the cosmological background [91, 122, 183]. Because of this reason, the amplitude of a GW can be damped differently compared to the one of an electromagnetic wave, leading to the relation Eq. (1.105), for the two luminosity distances. For later convenience, we rewrite such relation in terms of the EFT function $\Omega(a)$, as

$$\bar{d}_L^{\rm GW}(z) = \sqrt{1+\Omega(z)}\,\bar{d}_L^{\rm EM}(z)\,, \tag{3.1}$$

since, comparing the actions (1.62) and (1.68), it is clear that $M_P[\varphi_0(\tau)] = m_0\sqrt{1+\Omega(\tau)}$.

As the GW strain can be parameterized in terms of the redshifted masses of the binary objects, GW sources cannot probe independently the redshift of the source unless there is a known mass-scale or physical scale which can be used to break the degener-

acy between mass and redshift [206, 268–271]. For some GW sources, such as binary neutron stars (NS) [200, 203, 204, 272, 273], NS-BH [274, 275], stellar and intermediate mass binary black holes (BH) [276] and massive binary BHs [277–279] embedded in accretion disks, a detectable electromagnetic counterpart can potentially be observed and used to measure its redshift directly with a spectroscopic (or photometric) follow-up of the host galaxy. These sources are typically dubbed 'bright' sirens and are the ones we consider here.

3.2.1. Convergence estimators for Gravitational Waves

On their journey through the expanding Universe, photons and GWs encounter clumped matter structures which induces scale-dependent corrections to their luminosity distance, $\Delta d_L^{\rm GW}$ in Eq. (1.112). Depending on the angular scale and redshift, some of the relativistic effects can be dominant. For instance, in [280] it was shown that for GW sources at redshifts higher than ~ 0.5 WL convergence is the dominant correction, that can reach $\sim 5\%$ of the measured strain. This qualitative result was then confirmed in [281], as discussed in Chapter 2 (see Figure 2.1). Given its substantial magnitude, WL is also a valuable signal to be exploited, rather than only a source of error, to probe the growth history and pattern of the LSS in the Universe. As it can be observed from Eq. (1.113), WL convergence is an integrated effect, it builds up during the propagation. For this reason, we focus on GW sources at high redshift, reaching up to $z \simeq 2.5$, for which we approximate Eq. (1.112) to

$$\frac{\Delta d_L^{\rm GW}}{\bar{d}_L^{\rm GW}} \simeq -\kappa_{\rm GW}\,, \tag{3.2}$$

where $\kappa_{\rm GW}$ is the lensing convergence field of GWs, that for a population of sources reads

$$\kappa_{\rm GW}(\hat{n}) = -\frac{1}{2}\nabla_\theta^2\phi_L(\hat{n}) = -\int_0^{\chi}\frac{d\chi'}{\chi'}\int_{\chi'}^{\infty}d\chi_*\left(\frac{\chi_*-\chi'}{\chi_*}\right)\frac{dn_{\rm GW}}{d\chi_*}\nabla_\theta^2\,\Psi_W(\chi'\hat{n},z')\,, \tag{3.3}$$

where $dn_{\rm GW}/d\chi_*$ is the distribution of the GW sources, Ψ_W is the Weyl potential, related to the matter overdensity as in Eq. (1.73), and ∇_θ^2 indicates the 2D Laplacian with respect to the angle between the image and optical axis. Note that we are neglecting the shear deformations of the signal since these are subdominant in linear perturbation theory where WL mainly affects the magnification of the GWs. In the case of bright events, we construct an estimator to extract the WL convergence from GW data as follows

$$\hat{\kappa}_{\rm GW}(z,\hat{n}) \equiv 1 - \frac{d_L^{\rm GW}(z,\hat{n})}{\bar{d}_L^{\rm EM}(z)}\,, \tag{3.4}$$

namely as the fractional difference between the GW luminosity distance $d_L^{\rm GW}(z,\hat{n})$, inferred from the measurement of the GW strain, and the electromagnetic background luminosity distance $\bar{d}_L^{\rm EM}(z)$. Here, we take the latter as defined via Eq. (1.106)

by choosing a fiducial cosmological model for $E(z)$. Such an estimator can be biased in three ways: the experimental error on the $d_L^{\rm GW}(z,\hat{n})$ measurement, the error on the source redshift, or by a wrong choice of the cosmological model (i.e. biased values of the parameters in $E(z)$). To account for all the effects above we introduce three parameters $\epsilon_{\rm GW}$, ϵ_z and ϵ_c, and modify the convergence estimator as

$$\begin{aligned}\hat{\kappa}_{\rm GW} &= 1 - \frac{\sqrt{1+\Omega(z)}\,(1-\kappa_{\rm GW}+\epsilon_{\rm GW})}{(1+\epsilon_z+\epsilon_c)} \\ &\sim 1 - \sqrt{1+\Omega(z)}\,(1-\kappa_{\rm GW}+\epsilon_{\rm GW}-\epsilon_z-\epsilon_c+\kappa_{\rm GW}\epsilon_z+\kappa_{\rm GW}\epsilon_c)\,,\end{aligned} \tag{3.5}$$

where we linearized to first order in $\epsilon_{\rm GW}$, ϵ_z, and ϵ_c assuming they are all small. The estimator in (3.4) relies on the availability of source's redshift information, reason why we are limiting this analysis to bright GW events.

3.3. Tomographic Observables

We consider cross-correlations between the density field of galaxies, $\delta_{\rm g}$, the weak lensing convergence fields as measured by galaxies, $\kappa_{\rm g}$, and the weak lensing convergence field as measured by GW, $\kappa_{\rm GW}$. The angular power spectrum for the cross-correlations is (see Section 1.1.3)

$$C_\ell^{X_iY_j} = \int_0^{z_{\rm max}} \frac{{\rm d}z}{\chi^2(z)H(z)} W_{X_i}(k(\ell,z),z)\,W_{Y_j}(k(\ell,z),z)\,P_{\rm P}\,(k(\ell,z),z)\,, \tag{3.6}$$

where $X_i, Y_j = [\delta_{\rm g}, \kappa_{\rm g}, \kappa_{\rm GW}]$ at the ith and j-th tomographic bin, $P_{\rm p}(k) \propto A_{\rm s}(k/k_*)^{n_{\rm s}-1}$ is the primordial power spectrum, with $A_{\rm s}$ and $n_{\rm s}$ its amplitude and spectral index and k_* a pivot scale [3, 4]. We applied the Limber and flat-sky approximations [282–287], which sets $k(\ell,z) = (\ell+1)/\chi(z)$, which we call simply k. $W_{X_i}(k,z)$ is the window function for the observable X in the i-th tomographic bin. For galaxies, the window function can be written as

$$W^i_{\delta_{\rm g}}(k,z) = \mathcal{T}_\delta(k,z)\,b^i_{\rm g}(z)\,n^i_{\rm g}(z)\,H(z)\,, \tag{3.7}$$

where $\mathcal{T}_\delta(k,z)$ is the matter transfer function, evolving the primordial power spectrum such that $P_\delta(k,z) = \mathcal{T}^2_\delta(k,z)P_{\rm p}(k)$. In Eq. (3.7), $n^i_{\rm g}(z)$ and $b^i_{\rm g}(z)$ are, respectively, the galaxy redshift distribution and the linear galaxy bias in the i-th redshift bin which we model following [288]. The window function of the GW lensing convergence is

$$W^i_{\kappa_{\rm GW}}(k,z) = \mathcal{T}_{\Psi_W}(k,z)\int_z^\infty {\rm d}z'\,\frac{\chi(z')-\chi(z)}{\chi(z')}\,n^i_{\rm GW}(z')\,, \tag{3.8}$$

where $n^i_{\rm GW}(z)$ is the redshift distribution of GW sources in the i-th bin, and $\mathcal{T}_{\Psi_W}(k,z)$ is the Weyl potential transfer function, which allows to get its power spectrum

$P_{\Psi_W}(k,z) = T^2_{\Psi_W}(k,z)P_{\rm p}(k)$. The galaxy WL convergence window function is

$$W^i_{\kappa_{\rm g}}(k,z) = \mathcal{T}_{\Psi_W}(k,z)\int_z^\infty {\rm d}z'\,\frac{\chi(z')-\chi(z)}{\chi(z')}\,n^i_{\rm g}(z') + W^i_{\rm IA}(k,z)\,, \tag{3.9}$$

where, with respect to Eq. (3.8) we introduce an extra term $W^i_{\rm IA}(k,z)$ to include the Intrinsic Alignment (IA) systematic effect that we model following [288], *i.e.*

$$W^i_{\rm IA}(k,z) = -\mathcal{T}_\delta(k,z)\frac{A_{\rm IA}C_{\rm IA}\Omega_{\rm m,0}F_{\rm IA}(z)}{D(z)}\,n^i_{\rm g}(z)H(z)\,, \tag{3.10}$$

where $D(z)$ is the growth factor, $\Omega_{\rm m,0}$ the current matter density, and the subscript IA highlights the terms including the nuisance parameters $A_{\rm IA}$, $\beta_{\rm IA}$ and $\eta_{\rm IA}$, the last two being contained in the $F_{\rm IA}$ function, while $C_{\rm IA} = 0.0134$ is a fixed constant.

Scalar-tensor theories modify the growth pattern of perturbations, affecting differently the different observables. The window functions just described will be correspondingly modified, mainly through the transfer functions $\mathcal{T}_\delta(k,z)$ and $\mathcal{T}_{\Psi_W}(k,z)$, which encode the evolution of density perturbation and lensing potential, respectively. Modifications of the growth also affect the growth factor $D(z)$ entering the IA contribution to the power spectra. As discussed in Section 1.2.2, their analytic forms are too complicated to give explicitly, so that they are computed, once again, through the Einstein-Boltzmann solver code `EFTCAMB` [89, 90]. We also use the same code to produce the angular power spectra described in this section.

Finally, we model the distribution of sources (src) in each redshift bin as

$$n^i_{\rm src}(z) = \frac{dn_{\rm src}}{dz}\left[{\rm Erf}\left(\frac{z-z^i_-}{\sqrt{2}\sigma^{\rm src}_z(z)}\right) - {\rm Erf}\left(\frac{z-z^i_+}{\sqrt{2}\sigma^{\rm src}_z(z)}\right)\right], \tag{3.11}$$

with src = $\left[{\rm g}, {\rm GW}\right]$, z^i_- and z^i_+ the lower and upper limits of the i-th bin, $\sigma^{\rm src}_z(z)$ the error on the redshift measurement for the considered source, and $dn_{\rm src}/dz$ is parameterised as

$$\frac{dn_{\rm src}}{dz} \propto \left(\frac{z}{z_0}\right)^2 \exp\left[-\left(\frac{z}{z_0}\right)^{3/2}\right]. \tag{3.12}$$

The parameter z_0 entering Eq. (3.12), as well as the redshift error $\sigma^{\rm src}_z$ of Eq. (3.11), are survey dependent and we will specify them in the following Section (Sec. 3.4) where we introduce the surveys considered in this study.

In this Chapter, we focus on the GW lensing auto-correlation, $C_\ell^{\kappa_{\rm GW}\kappa_{\rm GW}}$, and its cross-correlations with galaxies, $C_\ell^{\kappa_{\rm GW}\delta}$ and $C_\ell^{\kappa_{\rm GW}\kappa_g}$. Using the estimator in Eq. (3.5), we can see that

$$\langle\hat{\kappa}_{\rm GW}\delta_{\rm g}\rangle \simeq \sqrt{1+\Omega}\langle\kappa_{\rm GW}\delta_{\rm g}\rangle\,, \tag{3.13}$$

$$\langle\hat{\kappa}_{\rm GW}\kappa_{\rm g}\rangle \simeq \sqrt{1+\Omega}\langle\kappa_{\rm GW}\kappa_{\rm g}\rangle\,, \tag{3.14}$$

$$\langle\hat{\kappa}_{\rm GW}\hat{\kappa}_{\rm GW}\rangle \simeq (1+\Omega)\langle\kappa_{\rm GW}\kappa_{\rm GW}\rangle + N_{\rm GW} + N_z, \tag{3.15}$$

where we have considered that the three sources of error $\{\epsilon_{\rm GW},\epsilon_z,\epsilon_c\}$ are not correlated between themselves or with either the convergence or the contrast density field. To derive the equations above, we have neglected terms of third order or higher in the perturbations, introduced the noise's power spectra $N_{\rm GW} = \langle\epsilon_{\rm GW}\epsilon_{\rm GW}\rangle$ and $N_z = \langle\epsilon_z\epsilon_z\rangle$, and used that $\langle\epsilon_{\rm GW}\rangle = \langle\epsilon_z\rangle = 0$ when the average is performed over large volumes. Contrary, in general $\langle\epsilon_c\rangle \neq 0$, hence in a complete analysis the term should be included. However, this correction is typically small, and we will assume the noise to be dominated by other terms, that we model in Sec. 3.4.

3.4. Models, methodology and surveys specifications

This section provides details of the gravitational models on which we forecast constraints, as well as the details on the analysis we performed to obtain them.

3.4.1. Models

We forecast the constraining power of GW-WL, alone and in combination with galaxy clustering and WL, on the cosmological parameters. We investigate gravitational models belonging to the Horndeski class of theories and described by the action of Eq. (1.68). We work in the *designer* approach [90], by fixing the background expansion history to a choice for the DE equation of state $w_{\rm DE}$ as explained in Section 1.2.2, so that any EFT model is fully specified after assigning the EFT functions $\{w_{\rm DE},\Omega,\gamma_1,\gamma_2\}$. We model the dark energy equation of state using the CPL parametrization [98, 99]

$$w_{\rm DE}(a) = w_0 + w_a(1-a) \tag{3.16}$$

as in Eq. (1.70). With this prescription, the continuity equation in Eq. (1.69), dictates that the background DE density evolves as

$$\rho_{\rm DE}(a) = \rho^0_{\rm DE} a^{-3(1+w_0+w_a)} e^{-3w_a(1-a)}, \tag{3.17}$$

with $\rho^0_{\rm DE} = \rho_{\rm DE}(a=1)$ its value today.

Then, we choose to parameterize the time dependencies of $\Omega(a)$ and $\gamma_2(a)$ as

$$\Omega(a) = \Omega_0 \frac{\rho_{\rm DE}}{\rho^0_{\rm DE}}, \qquad \gamma_2(a) = \gamma_2^0 \frac{\rho_{\rm DE}}{\rho^0_{\rm DE}}, \tag{3.18}$$

linking the modifications to ΛCDM to the DE energy density. This way, the effects of having $\Omega(a),\gamma_2(a) \neq 0$ become small in the early Universe, when matter or radiation are driving its expansion. Additionally, we set $\gamma_1 = 0$ for all models, given that it affects only negligibly linear perturbations in the range of our observables (see e.g. [289]). Based on these assumptions, we consider three scenarios:

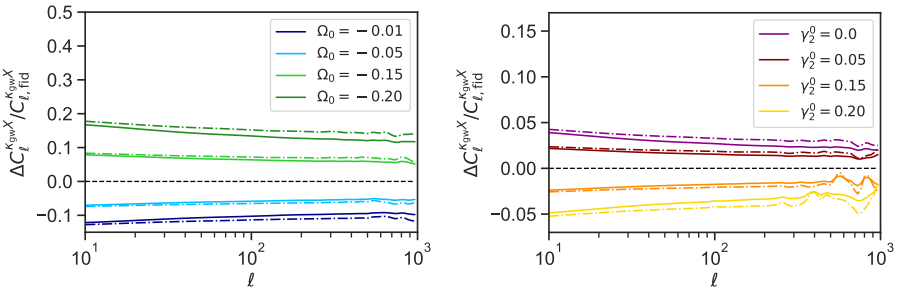

Figure 3.1: Relative deviations of the angular power spectrum, as a function of multipole ℓ for model M2. We plot in the left (right) panel how C_ℓ vary for different values of Ω_0 (γ_2^0), while keeping the remaining parameters fixed to their fiducial values in Table 3.1). The solid lines correspond to auto-correlations of GW-WL ($X = \kappa_{\rm GW}$), while the dashed lines is the cross-correlations of GW-WL with galaxy WL ($X = \kappa_g$).

- **ΛCDM:** we consider the EFT parameters fixed to reproduce the standard model, i.e. $w_0 = -1$ and $w_a = \Omega_0 = \gamma_2^0 = 0$. Consequently, the set of free parameters consists of $\{\Omega^0_{\rm CDM}, \Omega^0_{\rm b}, h, n_{\rm s}, \sigma_8\}$: the CDM and baryonic relative energy densities at present time, the reduced Hubble constant $h = H_0/100$, the spectral index of the primordial power spectrum, and the amplitude of the linear matter power spectrum measured at $8/h$Mpc, respectively.

- **Model I (M1):** we fix $\gamma_2^0 = 0$; thus, the cosmology is specified by the parameters of ΛCDM plus $\{w_0, w_a, \Omega_0\}$. This model is representative of the Generalized Brans-Dicke class: with a non-minimal coupling, but no derivative interaction ($\gamma_2^0 = 0$).

- **Model II (M2):** we fix $w_0 = -1.05$ and $w_a = 0$; thus, the cosmology is specified by the parameters of ΛCDM and $\{\Omega_0, \gamma_2^0\}$. This model is representative of the class of kinetic gravity braiding models [290], where the conformal coupling and the derivative coupling are both allowed ($\Omega \neq 0$, $\gamma_2 \neq 0$).

We sketch the impact of the EFT parameters on the $C^{XY}(\ell)$ in Figure 3.1, where we plot the relative difference $(C_\ell^{\kappa_{\rm GW}X} - C_{\ell,\rm fid}^{\kappa_{\rm GW}X})/C_{\ell,\rm fid}^{\kappa_{\rm GW}X}$ adopting model M2 and choosing as baseline the cross-correlation computed in the fiducial cosmology. We plot curves for $X = \kappa_{\rm GW}$ (solid lines) and $X = \kappa_{\rm g}$ (dashed lines) varying the value of Ω_0 in the left panel and γ_2^0 in the right panel, while all other parameters are kept fixed at the fiducial value (see Tab. 3.1). We observe that taking Ω_0 lower than the fiducial value acts to strengthen the signal, while values closer to zero (and hence, to the LCDM value for Ω_0) diminish the signal. On the contrary, higher values of γ_2^0 tend to dampen the signal, while values closer to 0 enhance it. We notice, however, that the correlations react more strongly to small variations in Ω_0 than to changes in γ_2^0. Indeed, the values chosen for the right panel of Figure 3.1 span the full range available to γ_2^0 in this model to ensure a stable theory, while causing only variations in the

cross-correlations of, at most, 5%.

3.4.2. Analysis method

To compute forecasts, we adopt the Fisher matrix formalism [288, 291], which allows us to obtain bounds on the free parameters of the analysis from the information matrix $\mathcal{F}_{\alpha\beta}$. Following [288], we define the Fisher matrix as

$$\mathcal{F}_{\alpha\beta} = \sum_{\ell=\ell_{\rm min}}^{\ell_{\rm max}} \frac{2\ell+1}{2} \sum_{i,j,m,n} \sum_{A,B,C,D} \frac{\partial C_{ij}^{AB}(\ell)}{\partial\theta_\alpha} \left[K^{-1}(\ell)\right]_{jm}^{BC} \frac{\partial C_{mn}^{CD}}{\partial\theta_\beta} \left[K^{-1}(\ell)\right]_{ni}^{DA}, \quad (3.19)$$

where α and β run over the set of free cosmological parameters θ, while A, B, C and D run over the density and convergence fields $[\delta_{\rm g}, \kappa_{\rm g}, \hat{\kappa}_{\rm GW}]$ and finally i, j, m and n run over all unique pairs of tomographic bins. By the Cramer-Rao inequality, the lower bound on the standard deviation for the parameter θ_α is

$$\sigma_\alpha = \sqrt{\Sigma_{\alpha\alpha}} \quad \text{with} \quad \Sigma_{\alpha\alpha} \equiv [\mathcal{F}^{-1}]_{\alpha\alpha}. \quad (3.20)$$

To compute our matrices we use `CosmicFish` [292, 293][1], that we extended to include GW weak lensing. The covariance matrix K is defined as

$$K^{A_iB_j}(\ell) = \frac{C^{A_iB_j}(\ell) + N^{A_iB_j}(\ell)}{\sqrt[4]{f_{\rm sky}^A f_{\rm sky}^B}}, \quad (3.21)$$

where f_{sky}^A is the sky fraction covered by the detector measuring the observable A, and N_{ij}^{AB} the noise of the correlation considered, which we model as

$$N^{\delta_i\delta_j}(\ell) = \frac{1}{\bar{n}_{\rm g}^i}\delta_{ij}, \quad (3.22)$$

$$N^{\kappa_{\rm g}^i\kappa_{\rm g}^j}(\ell) = \frac{\sigma_\epsilon^2}{\bar{n}_{\kappa_{\rm g}}^i}\delta_{ij}, \quad (3.23)$$

$$N^{\kappa_{\rm GW}^i\kappa_{\rm GW}^j}(\ell) = \frac{1}{\bar{n}_{\rm GW}^i}\left(\frac{\sigma_{d_L}^2}{d_L^2} + \frac{\sigma_s^2}{d_L^2}\right) e^{\frac{\ell^2\theta_{\rm min}^2}{8\ln 2}}\delta_{ij}, \quad (3.24)$$

where δ_{ij} is the Kronecker delta and $\bar{n}_A^i$ is the number of sources in the i-th redshift bin for the probe A. We assume also that the noises of different probes are uncorrelated. In the equations above, σ_ϵ represents the intrinsic ellipticity affecting shear measurements, σ_{d_L} represents the average experimental error on the luminosity distance of the GW sources, while $\sigma_s = (\partial d_L/\partial z)\,\sigma_z^{\rm GW}$ is the contribution to the luminosity distance error brought by the uncertainty on the merger redshift $\sigma_z^{\rm GW}$, where the propagation is obtained assuming a fiducial cosmology. Lastly, $\theta_{\rm min}$ is the sky-localization area of the GW event, which also dictates the maximum available multipole for the analysis.

[1] `CosmicFish` is publicly available at `https://cosmicfish.github.io/`.

Model	h	$\Omega_{m,0}$	$\Omega_{b,0}$	n_s	σ_8	w_0	w_a	Ω_0	γ_2^0
ΛCDM	0.6774	0.31	0.05	0.9667	0.8159	(-1.0)	(0.0)	(0.0)	(0.0)
Model I	0.6774	0.31	0.05	0.9667	0.8159	-1.1	-0.05	-0.1	(0.0)
Model II	0.6774	0.31	0.05	0.9667	0.8159	(-1.05)	(0.0)	-0.1	0.1

Table 3.1: Fiducial values for the parameters of the cosmological models considered. Round brackets around a value mean that the corresponding parameter is kept fixed during the Fisher analysis, while the remaining are constrained simultaneously. In addition, we also let the galaxy bias in each bin and the IA parameters free to vary, for which we use the same fiducial values as [288].

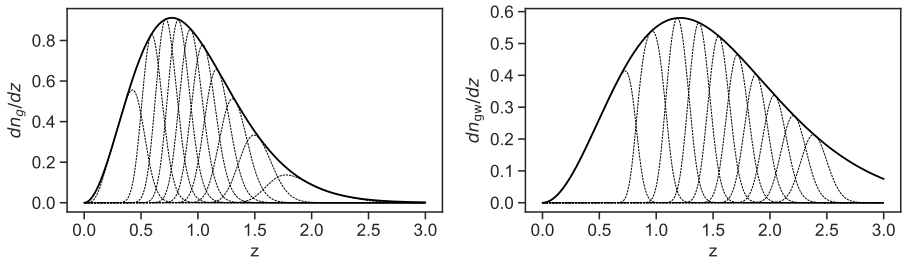

Figure 3.2: Normalized redshift distribution of galaxies and bright GW sources (left and right panel respectively). The dashed lines illustrate the redshift binning applied in our analysis.

3.4.3. Galaxy and GW surveys

We use the specifications of [288], as representative of a Stage IV galaxy survey, for the galaxy distribution in Eq. (3.12), and the fraction of sky observed. We instead take a simpler approach for the photometric redshift error, using Eq. (3.11) with $\sigma_z^{\rm g} = 0.03(1+z)$, from which we obtain the distribution of sources in ten equipopulated redshift bins with $z \in [0, 2.5]$. We use a minimum multipole $\ell_{\rm min} = 10$ for both galaxy clustering and weak lensing, while fix the maximum multipole to $\ell_{\rm max}^{\rm GC} = 750$ for the former and $\ell_{\rm max}^{\rm WL} = 1000$ for the latter, in line with the "pessimistic" scenario of [288], but with the further limitation in the weak lensing multipoles because of the lack of a consolidated recipe to deal with non-linearities in the Horndeski theory (1.62).

Concerning the GW survey, we opt for $z_0 = 1.5$ for the GW source distribution in Eq. (3.12): this way Eq. (3.12) is compatible with both the forecasts of [277] for LISA luminous massive black hole binaries, and of [273] for the binary neutron stars observed by a network of ET in combination with two CE detectors. The reason for choosing this parametrization is the attempt of remaining as detector a-specific as possible, while still modeling the sources' distribution to mimic forecasted future observations. As we match it to distributions of mock observed events, our source distribution automatically accounts for possible selection effects of both GW and EM detectors. As in the case of galaxies, we consider $z \in [0, 2.5]$ and bin the GW sources

in ten equipopulated redshift bins. We also explore different binning choices: we consider the cases with only eight and six equipopulated bins. We observe a very small deterioration in the cosmological constraints when decreasing the number of tomographic bins, as larger bins tend to smooth out the lensing signal, as we show in Section 3.5.3. However, our conclusions on the impact of GW-WL on the constraining power remains the same regardless of binning, thus in what follows we will report results only for the most favorable choice of 10 bins.

The main quantities that can impact the weak lensing estimation from bright GW sources are the uncertainty on the luminosity distance, the error on the source redshift and the total number of bright GW events. The peculiar velocity correction for sources at high redshift are going to be a less significant contamination [224]. We consider several possibilities for the total number of detected GW events, $N_{\rm GW}$, ranging from 10^3 to 10^6, while we vary the average precision on the luminosity distance, σ_{d_L}/d_L, from 10% down to 0.5%. We assume that the GW sources have an electromagnetic counterpart (or an identifiable host galaxy), whose redshift is measured either photometrically, with error $\sigma_z^{\rm GW} = 0.03(1+z)$, or spectroscopically, with error $\sigma_z^{\rm GW} = 0.0005(1+z)$ [79, 125]. In Figure 3.2 we show the normalized source distribution of galaxies (left panel) and bright GW events (right panel) adopted in this analysis, together with a representation of the redshift binning that is applied, and we summarize the specifications considered for galaxy and GW surveys in Table 3.2.

Since we are focusing on bright sirens, in Eq. (3.24) we set $\theta_{\rm min} = 0$, thus implying that the event is perfectly localized by identifying the EM counterpart. On the other hand, in our analysis we truncate the summation in Eq. (3.19) at $\ell_{\rm max} = 1000$ to match the limiting multipoles of the galaxy survey, which is equivalent to limit angular scales to $\theta_{\rm min} \sim 11\,$arcmin. Going up to larger $\ell_{\rm max}$ would result in an enhancement of the signal-to-noise ratio. This on one hand would imply tighter constraints on cosmological parameters when all sources are combined. At the same time, though, the GC and WL signal themselves would benefit from the accessibility of higher multipoles, resulting in tighter galaxy-only constraints to begin with. Thus, we can expect that, qualitatively, the impact of GW on the galaxy bounds remains similar even if higher multipoles are accessible.

3.5. Results

Using the specifications, models and methodology described in Sec. 3.4, we include in the Fisher matrix the contributions from all correlators C_ℓ^{XY} with X and Y in $[\delta_{\rm g}, \kappa_g, \hat{\kappa}_{\rm GW}]$, to explore the joint constraining power of GW-WL and galaxy surveys over cosmological parameters. We collect the fiducial values chosen for the parameters of the different models in Tab. 3.1, which are compatible with current bounds [4, 289]. Additionally, we choose the fiducial cosmology in such a way that

Galaxy Clustering						
$f_{\rm sky}^{\rm g}$	$\sigma_z^{\rm g}$	_	z_0	$\bar{n}_g$ [arcmin^{-2}]	$\ell_{\rm min}$	$\ell_{\rm max}$
0.35	$0.03(1+z)$		$0.9/\sqrt{2}$	30	10	750
Galaxy Weak Lensing						
$f_{\rm sky}^{\kappa_{\rm g}}$	$\sigma_z^{\rm g}$	σ_ϵ	z_0	$\bar{n}_{\kappa_{\rm g}}$ [arcmin^{-2}]	$\ell_{\rm min}$	$\ell_{\rm max}$
0.35	$0.03(1+z)$	0.3	$0.9/\sqrt{2}$	30	10	1000
Bright GW Weak Lensing						
$f_{\rm sky}^{\kappa_{\rm GW}}$	$\sigma_z^{\rm GW}$	$\sigma_{d_L}/d_L(\%)$	z_0	$N_{\rm GW}$	$\ell_{\rm min}$	$\ell_{\rm max}$
1	$0.03(1+z)$ $0.0005(1+z)$	$\in [0.5, 10]$	1.5	$\in [10^2, 10^6]$	10	1000

Table 3.2: Parameters of the noises (Eqs. (3.22), (3.23) and (3.24)) and binned source distributions (Eq. (3.11)) of the probes considered.

the parameters' values fall within the stable region of the models considered (identified via the stability sampler of `EFTCAMB`) and that the numerical derivatives, needed to obtain the Fisher matrices (3.19), can be performed without exiting this region.

To account for degeneracies, we vary all together the highest number of parameters possible, in each model, as described in Table 3.1. If a probe is not particularly sensitive to a certain parameter, if it is let free to vary, we marginalize over it instead of considering it fixed to its fiducial value. This is the case, for instance, of weak lensing: it is mostly sensitive to $\Omega_{\rm CDM}$ and σ_8, and doesn't depend much on other parameters such as the baryons' abundance. In addition, we always let free to vary the galaxy bias in each bin $b_{\rm g}^i$ and the IA parameters $A_{\rm IA}$, $\beta_{\rm IA}$ and $\eta_{\rm IA}$, for which we use the same fiducial values as [288].

3.5.1. Lambda CDM

Let us start with the ΛCDM scenario. In Figure 3.3 we show the marginalized 1σ relative bounds obtained on $\Omega^0_{\rm CDM}$ and σ_8 varying the total number of GW observations, $N_{\rm GW}$, and the luminosity distance precision σ_{d_L}/d_L. The first row shows the results considering photometric observations of the electromagnetic counterparts or of the GW host galaxy, while the second row assumes spectroscopic observations. For photometric observations, we notice that the bounds on both $\Omega^0_{\rm CDM}$ and σ_8 do not change for about half of the configurations considered (yellow regions in the plots), regardless of the choices made for the GW sector. In these regions, the bounds on cosmological parameters are strongly dominated by galaxies, contributing almost entirely to the constraining power. The black line marks the point

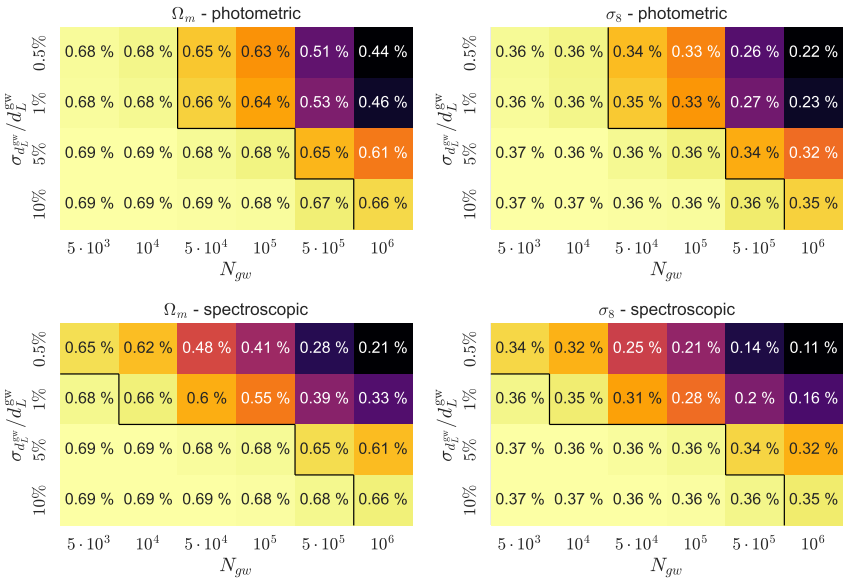

Figure 3.3: Marginalized 1σ relative confidence bounds for $\Omega^0_{\rm CDM}$ (left panel) and σ_8 (right panel) in ΛCDM. Top row: bright sirens with photometric redshift determination. Bottom row: similar with spectroscopic error. In all tables, bounds are derived from the combination of GW weak lensing, galaxies weak lensing and galaxy clustering, for different values of $N_{\rm GW}$ and $\sigma_{d_L^{\rm GW}}/d_L^{\rm GW}$.

at which GW events start to weight in significantly: about 5×10^5 bright sources with luminosity distance determined at least at 1% precision, or 10^6 sources with luminosity distance determined at 5% precision, or better, are necessary to witness a significant impact of GW-WL on the constraints already placed by galaxy probes. Similar considerations can be drawn for the spectroscopic case: GW becomes competitive with galaxies only for $N_{\rm GW} \geq 10^5$ for $\sigma_{d_L^{\rm GW}}/d_L^{\rm GW} \leq 1\%$ (or $N_{\rm GW} \geq 10^6$ for $\sigma_{d_L^{\rm GW}}/d_L^{\rm GW} \leq 5\%$). We can though recognize the reduced noise affecting GW lensing in the overall better performance of the spectroscopic sirens: for all configurations in which GW contributes significantly to the constraining power, spectroscopic sources always provide bounds up to 0.1% tighter than the photometric ones. For example, the 0.7% ($\sim 0.4\%$) bound placed on $\Omega^0_{\rm CDM}$ (σ_8) by galaxies can be reduced to 0.45% (0.2%) by factoring in the contribution of 10^6 photometric sirens measured with $\sigma_{d_L^{\rm GW}}/d_L^{\rm GW} = 1\%$, and further shrinked to $\sim 0.3\%$ (0.15%) considering instead the same number of spectroscopic events. Although we do not reproduce them here, we have performed the same analysis for the other free ΛCDM parameters, finding a similar behavior regarding the constraints on $n_{\rm s}$ (see also Figure 3.4). However, the impact of GW-WL on the constraints of h and Ω_b, remains mild for all configurations explored, since GW-WL is not particularly sensitive to those parameters.

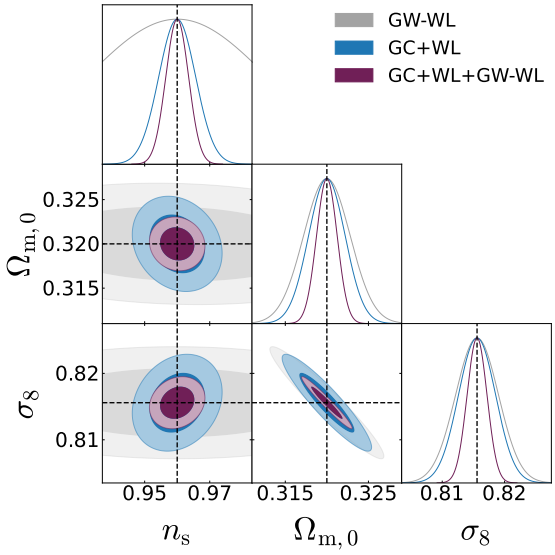

Figure 3.4: Marginalized forecasts for ΛCDM parameters. We fix $N_{\mathrm{GW}} = 5 \cdot 10^5$, $\sigma_{d_L^{\mathrm{GW}}}/d_L^{\mathrm{GW}} = 1\%$ and redshift information with spectroscopic error. Constraints come from GW weak lensing only (grey), galaxies WL and clustering (blue), and their combination (dark red).

In Figure 3.4 we show the triangular plots for three free parameters of ΛCDM, after having marginalized over h and Ω_b. In order to understand the extent of the impact of GW-WL, we opt for the scenario in which $N_{\mathrm{GW}} = 5 \cdot 10^5$ are detected with a precision of 1% on their luminosity distance measure and with a spectroscopic determination of the redshift. We plot bounds obtained considering GW-WL only, GC and galaxies WL, and the joint contribution of galaxy surveys and GW-WL. In the spectroscopic case, the GW-WL constraints on $\Omega_{m,0}$ and σ_8 are comparable with those coming from galaxies, and they halve when all probes are combined, also thanks to the reduced impact of nuisance parameters. On the contrary, GW-WL alone is not able to constrain n_s. When considering the probes all together, the bounds on σ_8 and Ω^0_{CDM} shrink, breaking also the mild degeneracy that exists in the galaxy-only constraints between the couple of parameters $(n_s, \Omega^0_{\mathrm{CDM}})$ and (n_s, σ_8). The net result is a strong reduction also of the bound on n_s. The analysis performed above shows that GWs, valuable because they provide independent measurements of the cosmological parameters, can improve the constraints induced by the other galaxy-related probes only if their statistical power (in terms of number of events and detection precision), is comparable with those of a galaxy survey. Indeed, in ΛCDM where the non-minimal coupling $\Omega(a) = 0$, the estimator in Eq. (3.4) corresponds to the same convergence measured by galaxy surveys. Hence, GW-WL and its cross-correlations with galaxies contributes to the constraining power only by effectively strengthening the WL statistics, in the case of the standard cosmological model.

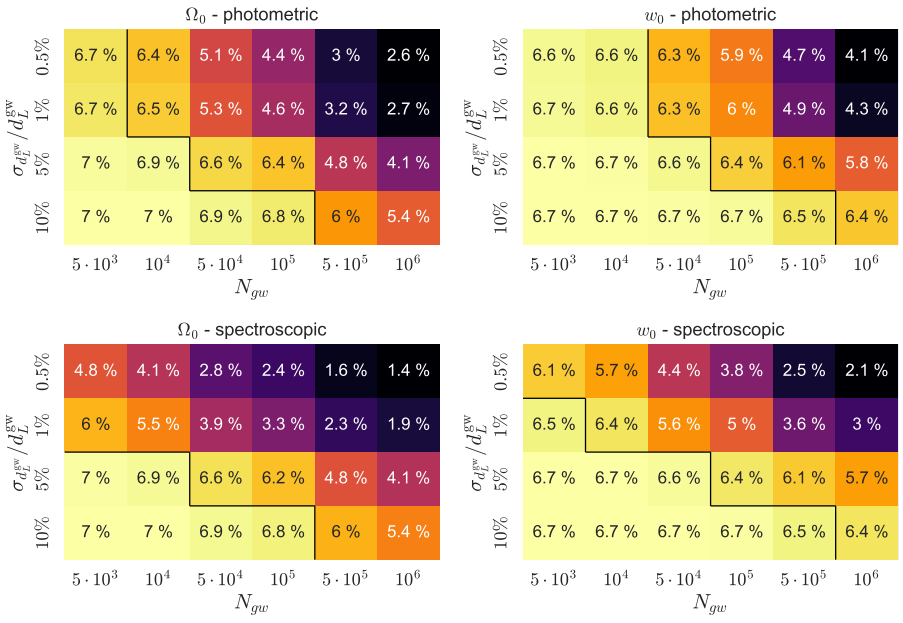

Figure 3.5: Marginalized 1σ confidence bounds on Ω_0 and w_0 parameters of Model I, obtained from combining GW weak lensing with galaxy weak lensing and clustering. We assume that all GW sources have a photometric (top panels) or spectroscopic (bottom panels) redshift determination.

3.5.2. Dark Energy models

We not turn our attention to Model I and Model II. In both cases, the estimator (3.4) receives explicit contributions from the conformal coupling $\Omega(a)$, making GW-WL effectively different from the corresponding galaxy probe. As before, we vary $N_{\rm GW}$, $\sigma_{d_L^{\rm GW}}/d_L^{\rm GW}$ and the error on the sources' redshift determination σ_z. For each combination, we compute the Fisher forecasts on the cosmological parameters, including all options of the kind C_ℓ^{XY}, $X, Y \in [\delta_g, \kappa_g, \hat{\kappa}_{\rm GW}]$.

In Figure 3.5 we show the marginalized 1σ bounds on Ω_0 and w_0 in M1, for the case of photometric (top row) and spectroscopic (bottom row) redshifts. Similarly to Figure 3.3, in the regions below the black line, the constraining power is mainly due to galaxy-probes. Contrary to ΛCDM, because of the definition of $\hat{\kappa}_{\rm GW}$ in Eq. (3.4), GW become more impactful for less daring configurations of $N_{\rm GW}$ and $\sigma_{d_L^{\rm GW}}/d_L^{\rm GW}$. In the case of photometric redshift, 5×10^4 GW sources determined with $\sigma_{d_L^{\rm GW}}/d_L^{\rm GW} \leq 1\%$ are already sufficient to detect a tightening of the constraints on w_0 and Ω_0. In the case of spectroscopic redshift information, for every value of $N_{\rm GW}$, there is at least one setup in which GWs improve the constraining power.

Figure 3.6 shows analogous tables for Ω_0 and γ_2^0 in the M2 case. Here, galaxy-

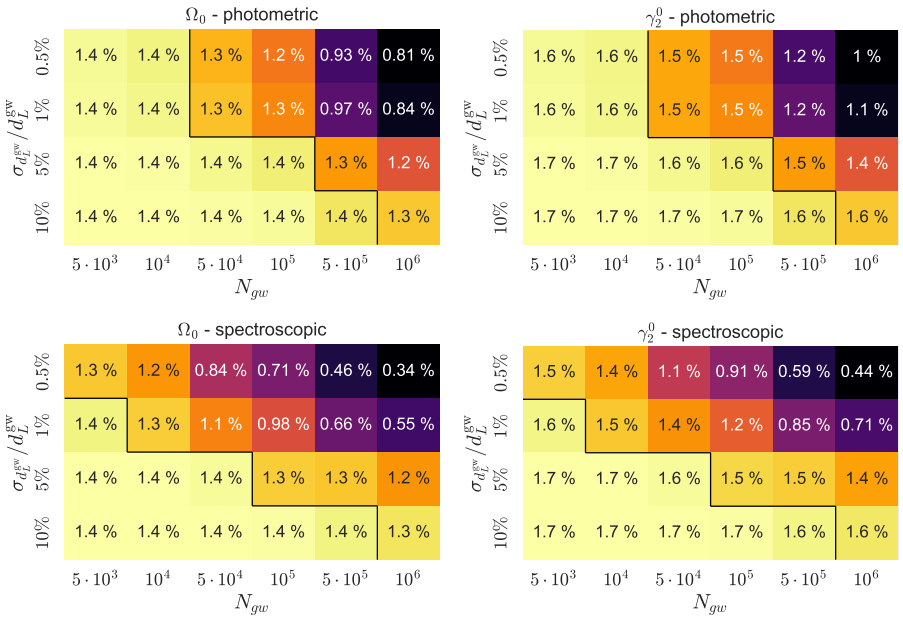

Figure 3.6: Marginalized 1σ confidence bounds on MG parameters obtained from combining GW weak lensing with galaxy weak lensing and clustering. We consider bright sirens and vary the number of GW detections $N_{\rm GW}$ and the precision on the luminosity distance determination σ_{d_L}. Bounds are reported for the parameters Ω_0 and γ_2^0 in our M2 model in the assumption that all GW sources will have a photometric (top panels) or spectroscopic (bottom panels) counterpart.

dominated constraints are tighter on the parameters than in the M1 case as $\{w_0, w_a\}$, affecting the background, are kept fixed. This allows for an overall easier determination of the value of the EFT functions today, which in turn requires higher $N_{\rm GW}$ for GW-WL to have an impact on cosmological bounds. In the photometric scenario, about $10^5 - 10^6$ sources are required to reach % and sub-% level precision on Ω_0, while the number drops to $N_{\rm GW} \sim 10^4 - 10^5$ in the spectroscopic case. In the photometric and spectroscopic cases, large enough statistics allows determining both parameters at the % and $\sim 0.4\%$ level.

In Figure 3.7 we report the triangular plots with marginalized constraints for some of the parameters of M1 (left panel) and M2 (right panel). We opt for the scenario in which $5 \cdot 10^5$ GW events are detected with a spectroscopic bright counterpart and their luminosity distance is determined at 1% accuracy. The left panel of Figure 3.7 highlights that the GW-only contours are still remarkably wide with respect to the galaxy ones. We show this more evidently in the left panel of Figure 3.8, where we plot the GW-WL only constraints in gray compared to the GC+WL constraints in blue.

The reason behind this, that GW-WL alone is not a good probe to constrain the DE

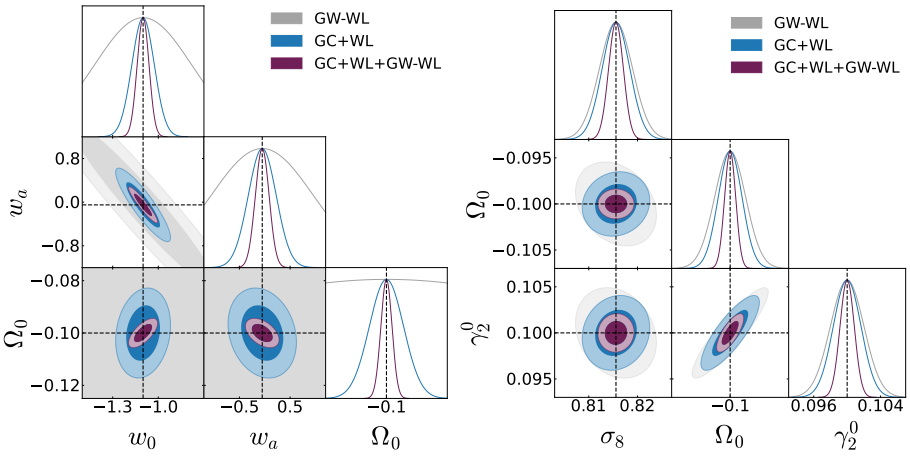

Figure 3.7: Marginalized forecasts for the MG parameters of model M1 (left panel) and M2 (right panel) in an idealistic scenario where $5 \cdot 10^5$ GWs events are detected with a bright counterpart measured spectroscopically, and luminosity distance measured with 1% precision. Constraints come from GW weak lensing only (gray), galaxies WL and clustering (blue), and GW and galaxy probes combined, including cross-correlations between the probes (purple).

equation of state, and the poor determination of $w_{\rm DE}$ leaves the coupling evolution unconstrained (see Eq. (3.18)), resulting in very loose bounds on Ω_0. Regardless of this, the combined GW+galaxy constraints (dark red contours in Figure 3.7) on the EFT parameters of M1 are narrower than the galaxy-only bounds. This increase of constraining power must come from the cross-correlations $C_\ell^{\kappa_{\rm GW}\delta}$ and $C_\ell^{\kappa_{\rm GW}\kappa_{\rm g}}$, as it can be seen in the right panel of Figure 3.8, where we compare the marginalized bounds of the galaxies with the contours obtained including only GW-WL and its two cross-correlations with the galaxy fields (GW-WL+XC, brown contours). The joint power of GW-WL with, in particular, GC is breaking (or mitigating) the degeneracies in the DE parameters sector, shrinking the constraints. This confirms the essential role that GW-WL cross-correlations can have in impacting cosmological bounds.

As for model M2 (right panel in Figure 3.7) we see that constraints from GW-WL alone are much tighter than in M1: here w_0 and w_a are fixed so that their degeneracies with others EFT parameters are canceled. As the bounds are comparable with those coming from galaxies, we conclude that the role of GW-WL cross-correlations in this case is less significant, and the GW-WL auto-correlation already concurs to the overall constraining power. GW-WL intervenes, though, to break the mild degeneracies present in the GC+WL bounds between (Ω_0, γ_2^0) and σ_8. Accordingly, bounds on σ_8 are narrowed thanks to the GW contribution.

Note that in model I and II, the ΛCDM parameters $\{h, \Omega_{m,0}, \Omega_{b,0}, n_s, \sigma_8\}$ are still present. In both cases we find similar results to those of Section 3.5.1, *i.e.* $\mathcal{O}(10^5)$

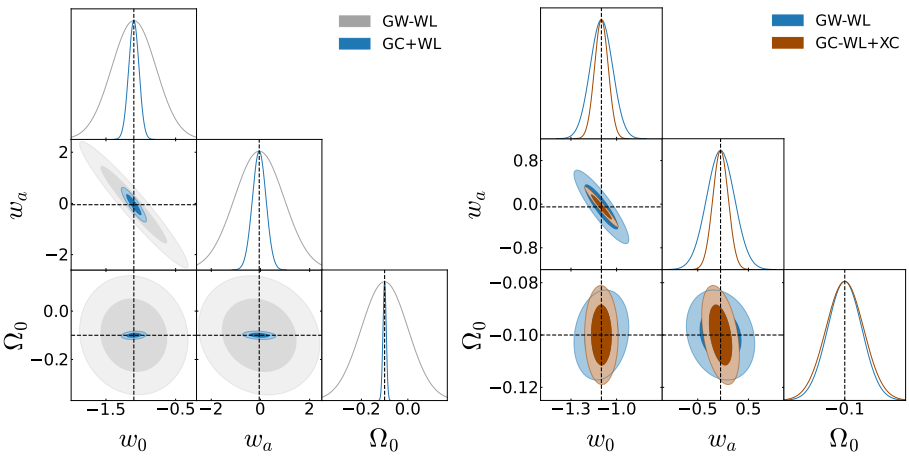

Figure 3.8: Comparison of the marginalized 1σ bounds on the MG parameters of M1. We consider the same setup of Figure 3.7, i.e. $N_{\rm GW} = 5 \cdot 10^5$, $\sigma_{\rm d_L} = 1\%$ and spectroscopic counterparts. In both panels, the blue contours represent bounds placed through GC+WL only, matching the same blue contours of the left panel of Figure 3.7. In the left panel, these are compared with GW-WL-only bounds, zooming out with respect to Figure 3.7 to include the full extent of the grey contours. In the right panel instead, the blue contours are confronted with bounds obtained considering only the auto-correlation of GW-WL and its cross-correlations with galaxies (brown regions), while not including GC+WL auto and cross-correlations.

or more GW sources are needed to even to impact significantly the bounds placed on those by galaxies alone, $\mathcal{O}(10^6)$ in the case of h and Ω_b. For a better comparison of the results obtained with different setups, we consider a Figure of Merit (FoM)

$$\text{FoM} = \det(\mathcal{F}_{\alpha,\beta})^{\frac{1}{2\text{N}}}\,, \tag{3.25}$$

where $\mathcal{F}_{\alpha,\beta}$ is the Fisher matrix of Eq. (3.19) marginalized over the bias and IA noise parameters, and N is the total number of parameters of the model [294]. The FoM is the 2N-th root of the product of the Fisher matrix eigenvalues, so it is inversely proportional to the volume of the N-dimensional ellipsoid delimiting the 1σ confidence region in the parameter space. The FoM thus allows us to investigate and quantify how the volume of the bounds in the parameter space is reduced when, for example, the statistics of the GW's event is increased. We compute the FoM (see Figure 3.9) for the Fisher matrices (3.19) of models M1 and M2, including all auto and cross-correlations of GW-WL, GC and galaxy WL and for all scenarios explored above in terms of $N_{\rm GW}$ and $\sigma_{\rm d_l}$. We also considered separately the cases in which GW events redshifts are determined photometrically or spectroscopically. From Figure 3.9, considering the photometric cases (top row), we see that FoM start increasing significantly from $N_{\rm GW} = 5 \times 10^4$ for all choices of σ_{d_L}, though it performs significantly better for $\sigma_{d_L} \leq 1\%$. The small difference between the curves for $\sigma_{d_L} \leq 1\%$ and $\sigma_{d_L} \leq 0.5\%$ suggests that the photometric redshift error is starting to dominate the correlation noise in Eq. (3.24): improving the d_L measurement of photometric

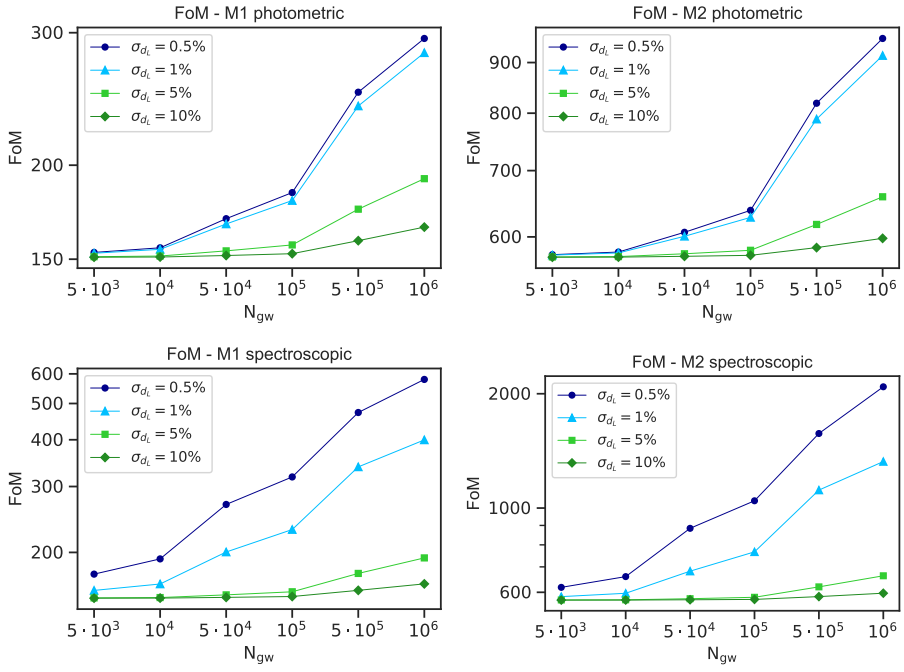

Figure 3.9: Figures of merit for different numbers of total detected events $N_{\rm GW}$ and several choices of $\sigma_{d_L^{\rm GW}}/d_L^{\rm GW}$. The top row displays results considering a spectroscopic redshift determination, while the bottom row those in case of photometric error. The left panels refer to M1, while the right panels to M2.

events beyond the 1% accuracy level only implies a minor increase in the GW-WL constraining power, and one should opt in maximizing the number of detections. On the contrary, because the redshift error is lower, for spectroscopic events the correlation noise remains dominated by σ_{d_L}, and improvements to the FoM happen for every choice of the latter. The FoM for model M1 are, in general, much lower than those of M2. This reflects our previous considerations on how placing tight constraints on model M1 is more difficult, because the EFT functions on M1 have higher freedom as their time evolution is not fixed, and there are higher degeneracies between the EFT parameters.

3.5.3. Impact of GW binning

To investigate the role of binning, we compare the FoM also for different configurations of their choice, for different values of $N_{\rm GW}$ and relative error on the luminosity distance measure. More in details, we consider 6, 8 and 10 equipopulated tomographic bins as described in Section 3.4.3. The results are reported in Figure 3.10, where we plot the ration of the FoM for all observational scenarios in the case of 6

bins (left panel), and 8 bins (right panel), over the configuration with 10 bins, i.e. $\mathrm{FoM}_n/\mathrm{FoM}_{10}$. Reducing the number of bins, in all cases, implies a lower FoM so a deterioration of the constraints on the cosmological parameters: decreasing the bins number, and thus increasing the bins size, has the effect of smoothing out the correlation signal in any given bin. This effect is compensated by a greater number of events falling in each bin, that attenuates the correlation noise of Eq. (3.24). In general, the FoM depends mildly on the number of bins. Higher deviations occur for higher numbers of detected events and better accuracy on the luminosity distance measurement, though we notice that even in the most extreme case of 6 tomographic bins and 10^6 GW events with d_L detected at 1% accuracy, FoM_6 is lower than FoM_{10} only of $\sim 1\%$. Therefore, our choice of 10 bins for the GW sources does not affect significantly the results presented previously.

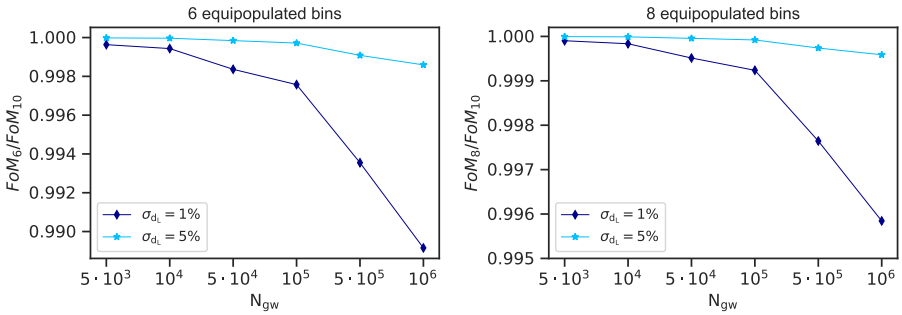

Figure 3.10: Ratio $\mathrm{FoM}_{[6,8]}/\mathrm{FoM}_{10}$ of the FoM computed binning the GW sources in 10 equipopulated tomographic bins and the FoM obtained for the same configurations in terms of number of GW sources N_{GW} and percentage uncertainty on the luminosity distance σ_{d_L}, but with a different number of bins (6 and 8 in the left and right panel respectively). The results regard the model M1.

3.6. Discussion and Conclusions

In this Chapter, we focused our attention to the weak-lensing signature on the estimates of the GW luminosity distances in Eq. (1.112), using it as a signal to investigate gravity on cosmological scales. We built the estimator $\hat{\kappa}_{\mathrm{GW}}$ in Eq. (3.4), as a proxy for the GW-WL field, which we will be able to extract from detections of sources at high-enough redshift ($z \geq 0.5$), where WL is the main relativist effect. This estimator, in the case of DE theories with a running Planck's mass, receives a contribution from the conformal coupling, making it even more interesting in the context of tests of the standard cosmological model. When focusing exclusively on ΛCDM, GW-WL can still provide an important information channel to constrain the cosmological parameters, as the contribution of GW increases the WL statistics. We have explored extensively the cross-correlations between $\hat{\kappa}_{\mathrm{GW}}$ and standard galaxy density fields δ_g and galaxy weak lensing κ_g, providing the observational requirements, in terms

of number of detected events and precision of each measurement, for future GW detectors to make stringent constraints on late time cosmological models, reaching beyond the limits that will be placed by the next generation of galaxy surveys. Focusing only on observations with a redshift information, we also distinguished the cases for which this is known with a photometric or spectroscopic measure.

We find that in the ΛCDM case, GW-WL starts to improve on galaxy-only constraints on σ_8 and $\Omega^0_{\rm CDM}$ if at least $\mathcal{O}(10^5)$ events are detected. When the DE parameter space is included, the situation becomes model dependent, as different EFT parameters can break (or not) different degeneracies. This is the main difference between Model I and Model II: WL alone is not particularly sensitive to the late time expansion history, so that whenever $w_{\rm DE}$ is left free to vary (as in M1 compared to M2), the bounds on the conformal coupling today Ω_0 are very large, given also its parametrization in Eq. (3.18). Nevertheless, the degeneracy between $\{w_{\rm DE}, \Omega_0\}$ in WL is broken when introducing the cross-correlations with also galaxy WL and galaxy clustering. This means that the constraining power of M1 are boosted when considering these probes together, and more reasonable values of $N_{\rm GW}$ and $\sigma_{d_L^{\rm GW}}$ are needed, while those of M2 scale down in a less pronounced way only because of the increased statistics. The specific numbers of $N_{\rm GW}$ and $\sigma_{d_L^{\rm GW}}$ needed in order for the GWs to actively participate in the constraining power can be found in Tables 3.3, 3.5 and 3.6, for ΛCDM, M1 and M2 respectively. The forecasts presented in this Chapter can be improved, for instance, by considering the cross-correlation signal up to higher $\ell_{\rm max}$, provided that a solid method to treat non-linearities is available.

To put the presented numbers in perspective, the network detector network of Einstein Telescope and (one or two) Cosmic Explorer place the number of observed bright binary neutron stars at few thousands of events per year [18, 273, 295], with forecasted error on luminosity distance of about 10% [273, 295]. We must however remark that, according to the cited estimates, ET is not expected to reach the average ∼ 1% accuracy on the luminosity distance determination required by our more promising setups (see e.g. Figs. 3.5 and 3.6), likely not even in combination with 2 CE detectors. An average accuracy over d_L of ∼ 10% could still lead to improvements on the galaxy-only cosmological constraints, but in that case we found that, for this to happen, $O(10^6)$ GW sources are required. Stacking a large statistics of highly accurate GW events will be possible with proposed far future observatories like the space-based Big Bang Observer [26] and Advanced Laser Interferometer Antenna [245], expected to reach sub-percent precision in the determination of the luminosity distance and with a total number of detected events of several hundreds of thousands. These detectors are also expected to have a high angular resolution [26, 245], facilitating the task of finding an electromagnetic counterpart or the host galaxy, needed for the redshift.

In conclusion, we find that the cross-correlations of galaxies and GW-WL have the

potential to become, with time, crucial probes of cosmology, complementary to galaxy surveys and other cosmological observables. Where sufficient statistics is available, this new probe can both help tighten constraints and strongly reduce existing degeneracies between the EFT parameters.

Note: My scientific contribution to the work presented in this Chapter regards the theoretical aspects. I've also had a mentoring role, introducing the first author to `EFTCAMB` and writing the scripts employed in the first explorations of the work. In particular, we used the version of the code we updated for *Detecting Dark Energy Fluctuations with Gravitational Waves*, namely Chapter 2. I also contributed in writing the paper.